nature portfolio

https://doi.org/10.1038/s41566-021-00901-z

Supplementary information

Quantum optics of soliton microcombs

In the format provided by the authors and unedited

Supplementary Information for Quantum Optics of Soliton Microcombs

Melissa A. Guidry*,[1], Daniil M. Lukin*,[1], Ki Youl Yang*,[1], Rahul Trivedi[1,2] and Jelena Vučković†,[1]

[1]E. L. Ginzton Laboratory, Stanford University, Stanford, CA 94305, USA.

[2]Max-Planck-Institute for Quantum Optics, Hans-Kopfermann-Str. 1, 85748 Garching, Germany

CONTENTS

I. LINEARIZED MODEL OF THE SOLITON MICROCOMB

In this section, we detail the linearized model and the calculation of second-order photon correlations. First, we begin with a general quartic Hamiltonian for a Kerr resonator with a single pump; we linearize the model to produce a quadratic Hamiltonian, where modes are coupled through the classical amplitudes which can be described by the LLE[S1]. Next, we define the input-output equations for the open quantum system, which we use to calculate the second-order correlation functions in a below-threshold comb. We numerically model the experiment of Fig. 3 from the main text to demonstrate the interface of the LLE with the input-output formalism. We then extend our model to describe photon correlations in the presence of bichromatic coherent light. Finally, we describe how to characterize entanglement (the logarithmic negativity, E_N) between different cavity modes starting from the Heisenberg equations.

A. Linearization

We consider the most general system Hamiltonian for four-wave mixing between cavity modes with coherent drive of the pump mode, $\mu = 0$:

$$\hat{H}_{\text{sys}} = \sum_{\mu} \omega_\mu \hat{a}_\mu^\dagger \hat{a}_\mu - \frac{1}{2} g_0 \sum_{\mu,\nu,j,k} \delta[\mu+\nu-j-k] \hat{a}_\mu^\dagger \hat{a}_\nu^\dagger \hat{a}_j \hat{a}_k + \alpha_0 (\hat{a}_0 e^{i\omega_p t} + \hat{a}_0^\dagger e^{-i\omega_p t}) \tag{1}$$

where $\delta[\mu+\nu-j-k]$ is the Kronecker delta which enforces the four-wave mixing mode-matching condition. Here, ω_μ is the resonance frequency of cavity mode μ and ω_p is the frequency of the coherent pump driving the central mode. The nonlinear coupling coefficient

$$g_0 = \frac{\hbar \omega_p^2 c n_2}{n_0^2 V_{\text{eff}}}$$

represents the per photon frequency shift of the cavity due to the third-order nonlinearity of the cavity: $\hbar$ is the reduced Planck's constant, n_2 is the nonlinear refractive index, n_0 is the material index, and V_{eff} is the effective mode volume of the resonator. The amplitude of the drive field is

$$\alpha_0 = \sqrt{\frac{\kappa_c P_{\text{wg}}}{\hbar \omega_p}}$$

where κ_c is the coupling rate of the cavity to the input waveguide and P_{wg} is the power in the input waveguide. To linearize the system, we write a formal separation of the optical state into the mean field solution (assumed to be a coherent state) and the quantum fluctuations: $\hat{a}_\mu(t) \to \alpha_\mu(t) + \hat{a}_\mu(t)$, where $\alpha_\mu(t)$ is the complex amplitude of the coherent state inside the cavity. Moving into the reference frame which removes explicit time dependence from the classical coupled mode equations[S2], we apply a unitary transformation using $\hat{U}(t) = e^{i\hat{R}t}$ where $\hat{R} = \sum_\mu (\omega_p + D_1\mu)\hat{a}_\mu^\dagger \hat{a}_\mu$. We enter the rotating frame of an evenly-spaced frequency ruler, with spacing D_1, centered at the central pump mode. Defining $\delta_\mu = \omega_\mu - \omega_p - D_1\mu$, and keeping only quadratic terms, we arrive at a Hamiltonian which includes the interaction Hamiltonian Eq. (1) of the main text:

$$\hat{H}_{\text{sys}} = \sum_{\mu} \delta_\mu \hat{a}_\mu^\dagger \hat{a}_\mu - \frac{g_0}{2} \sum_{\mu,\nu,j,k} \delta[\mu+\nu-j-k] (\overbrace{A_\mu A_\nu \hat{a}_j^\dagger \hat{a}_k^\dagger}^{\text{spontaneous pair generation}} + \underbrace{A_k^* A_\nu \hat{a}_j^\dagger \hat{a}_\mu}_{\text{XPM \& Bragg scattering}} + \text{h.c.}) \tag{2}$$

where A_μ are the complex-valued field amplitudes, described using the Lugiato-Lefever equation[S1]. The last term describes cross-phase modulation (XPM) when $\mu = j$, and four-wave mixing Bragg scattering otherwise.

B. Input-output formalism

The following calculations are in the Heisenberg picture. To describe the open system, we allow our cavity modes to couple to a bath. For a resonator with a large finesse, a Markovian approximation can be made on each mode

independently

$$H_{\text{bath}} = \sum_{\mu} \int \omega \hat{b}_{\mu}^{\dagger}(\omega)\hat{b}_{\mu}(\omega)d\omega \tag{3}$$

with a bath-coupling Hamiltonian

$$V = \sum_{\mu} \sqrt{\frac{\kappa_{\mu}}{2\pi}} \int \hat{a}_{\mu}^{\dagger}(\omega)\hat{b}_{\mu}(\omega)d\omega \tag{4}$$

where κ_{μ} is the total loss rate for cavity mode μ. Starting from the Hamiltonian $H = H_{\text{sys}} + H_{\text{bath}} + V$, we use the Heisenberg equations of motion $\dot{\hat{a}}_{\mu} = -i[\hat{a}_{\mu}, \hat{H}]$ to write down quantum coupled mode equations for this system which resemble the classical coupled mode equations:

$$\begin{aligned}\frac{d\hat{a}_{\mu}(t)}{dt} = &-\left(i\delta_{\mu} + \frac{\kappa_{\mu}}{2}\right)\hat{a}_{\mu}(t) + ig_0 \sum_{\nu,j,k} \delta[\mu + \nu - j - k]A_j A_k \hat{a}_{\nu}^{\dagger}(t) \\ &+ 2ig_0 \sum_{\nu,j,k} \delta[\mu + j - \nu - k]A_j^{*} A_k \hat{a}_{\nu}(t) - i\sqrt{\kappa_{\mu}}\hat{b}_{\text{in},\mu}(t)\end{aligned} \tag{5}$$

Each bath-cavity mode pair has an associated input-output relation:

$$\hat{b}_{\text{out},\mu}(t) = \hat{b}_{\text{in},\mu}(t) - i\sqrt{\kappa_{\mu}}\hat{a}_{\mu}(t) \tag{6}$$

We define the following $2n$-dimensional vectors describing n quantum modes in the frequency domain:

$$\bar{a}(\omega) = \begin{bmatrix} \hat{a}_1(\omega) \\ \vdots \\ \hat{a}_n(\omega) \\ \hat{a}_1^{\dagger}(-\omega) \\ \vdots \\ \hat{a}_n^{\dagger}(-\omega) \end{bmatrix} \qquad \bar{b}_{\text{in}}(\omega) = \begin{bmatrix} \hat{b}_{\text{in},1}(\omega) \\ \vdots \\ \hat{b}_{\text{in},n}(\omega) \\ \hat{b}_{\text{in},1}^{\dagger}(-\omega) \\ \vdots \\ \hat{b}_{\text{in},n}^{\dagger}(-\omega) \end{bmatrix} \qquad \bar{b}_{\text{out}}(\omega) = \begin{bmatrix} \hat{b}_{\text{out},1}(\omega) \\ \vdots \\ \hat{b}_{\text{out},n}(\omega) \\ \hat{b}_{\text{out},1}^{\dagger}(-\omega) \\ \vdots \\ \hat{b}_{\text{out},n}^{\dagger}(-\omega) \end{bmatrix} \tag{7}$$

We can define a matrix $N(\omega)$ from our coupled mode equations relating the output fluctuations to the input fluctuations:

$$\bar{b}_{\text{out}}(\omega) = N(\omega)\bar{b}_{\text{in}}(\omega) \tag{8}$$

C. Second-order photon correlations below threshold

We derive analytic expressions for two-photon correlations between quantum modes which interact with a single pumped mode[S3]. In this case, our Hamiltonian is simple, and we only consider interactions between pairs of modes $(-\mu, +\mu)$ centered around the pump. In this section, modes $(-\mu, +\mu)$ are represented by $(-, +)$ for conciseness. For this analysis, we choose $D_1 = (\omega_+ - \omega_-)/2\mu$ for which $\delta_+ = \delta_- = \delta$.

$$\hat{H}_{\text{sys}} = \delta(\hat{a}_-^{\dagger}\hat{a}_- + \hat{a}_+^{\dagger}\hat{a}_+) + ig(\hat{a}_-\hat{a}_+ - \hat{a}_-^{\dagger}\hat{a}_+^{\dagger}) \tag{9}$$

where $g = g_0|A_0|^2$, which includes both the Kerr coupling strength and the intensity in the pumped cavity mode. Assuming $\kappa_+ = \kappa_- = \kappa$, the Heisenberg equations read

$$\frac{d\hat{a}_{\pm}(t)}{dt} = -\left(i\delta + \frac{\kappa}{2}\right)\hat{a}_{\pm}(t) - g\hat{a}_{\mp}^{\dagger}(t) - i\sqrt{\kappa}\hat{b}_{\text{in},\pm}(t) \tag{10}$$

which gives us the following matrix $N(\omega)$:

$$N(\omega) = \begin{pmatrix} 1+\frac{\kappa(\kappa/2-i(\delta+\omega))}{(g^2-\delta^2)-(\kappa/2-i\omega)^2} & 0 & 0 & \frac{g\kappa}{(g^2-\delta^2)-(\kappa/2-i\omega)^2} \\ 0 & 1+\frac{\kappa(\kappa/2-i(\delta+\omega))}{(g^2-\delta^2)-(\kappa/2-i\omega)^2} & \frac{g\kappa}{(g^2-\delta^2)-(\kappa/2-i\omega)^2} & 0 \\ 0 & \frac{g\kappa}{(g^2-\delta^2)-(\kappa/2-i\omega)^2} & 1+\frac{\kappa(\kappa/2+i(\delta-\omega))}{(g^2-\delta^2)-(\kappa/2-i\omega)^2} & 0 \\ \frac{g\kappa}{(g^2-\delta^2)-(\kappa/2-i\omega)^2} & 0 & 0 & 1+\frac{\kappa(\kappa/2+i(\delta-\omega))}{(g^2-\delta^2)-(\kappa/2-i\omega)^2} \end{pmatrix}$$

We calculate the two-photon correlation function, represented in the general form for any two modes (i, j) as:

$$g_{ij}^{(2)}(t+\tau,t) = \frac{G^{(2)}(t+\tau,t)}{\left\langle \hat{b}_{\mathrm{out,i}}^{\dagger}(t)\hat{b}_{\mathrm{out,i}}(t)\right\rangle \left\langle \hat{b}_{\mathrm{out,j}}^{\dagger}(t+\tau)\hat{b}_{\mathrm{out,j}}(t+\tau)\right\rangle} \tag{11}$$

where

$$G^{(2)}(t+\tau,t) = \left\langle \hat{b}_{\mathrm{out,i}}^{\dagger}(t)\hat{b}_{\mathrm{out,j}}^{\dagger}(t+\tau)\hat{b}_{\mathrm{out,j}}(t+\tau)\hat{b}_{\mathrm{out,i}}(t)\right\rangle. \tag{12}$$

The expectation value is taken with respect to the initial vacuum state. The time-domain output bath operator is related to the frequency-domain input bath operator via:

$$\hat{b}_{\mathrm{out,i}}(t) = \frac{1}{\sqrt{2\pi}}\int_{-\infty}^{\infty} d\omega e^{-i\omega t}\hat{b}_{\mathrm{out,i}}(\omega) = \frac{1}{\sqrt{2\pi}}\int_{-\infty}^{\infty} d\omega e^{-i\omega t}\sum_{k=1}^{n}\left(N_{ik}(\omega)\hat{b}_{\mathrm{in,k}}(\omega) + N_{i(k+n)}(\omega)\hat{b}_{\mathrm{in,k}}^{\dagger}(-\omega)\right) \tag{13}$$

From here, $g_{ij}^{(2)}(t+\tau,t)$ may be calculated using the commutation relations of the frequency-domain input bath operators:

$$\left\langle \hat{b}_{\mathrm{in,i}}(\omega)\hat{b}_{\mathrm{in,j}}^{\dagger}(-\omega')\right\rangle = \delta_{ij}\delta(\omega+\omega') \qquad \left\langle \hat{b}_{\mathrm{in,i}}^{\dagger}(-\omega)\hat{b}_{\mathrm{in,j}}(\omega')\right\rangle = 0$$

After applying the commutation relations for modes ($-$, $+$), one arrives at an expression where each term is a product of Fourier transforms. Defining $\lambda = \sqrt{g^2-\delta^2}$, the result is:

$$g_{++}^{(2)}(\tau) = 1 + \frac{e^{-\kappa\tau}}{\lambda^2}\left[\frac{\kappa}{2}\sinh(\lambda\tau) + \lambda\cosh(\lambda\tau)\right]^2 \tag{14}$$

$$g_{+-}^{(2)}(\tau) = 1 + \frac{e^{-\kappa\tau}}{g^2}\left|\left(\lambda - i\frac{\kappa}{2}\frac{\delta}{\lambda}\right)\sinh(\lambda\tau) + \left(\frac{\kappa}{2} - i\delta\right)\cosh(\lambda\tau)\right|^2 \tag{15}$$

and $g_{++}^{(2)}(\tau) = g_{--}^{(2)}(\tau)$, $g_{+-}^{(2)}(\tau) = g_{-+}^{(2)}(-\tau)$.

D. Numerical analysis of OPO threshold

To compute the second-order correlation matrix of the quantum optical fields in the presence of the above-threshold Kerr comb, we combine the LLE simulation with input-output theory[S2]. The basic test case for the self-consistency of the joint LLE and input-output modelling is the OPO threshold condition: specifically, when the laser is tuned from blue to red to model the experiment, the asymptotic bandwidth narrowing in the below-threshold mode (as computed via input-output theory) and the formation of primary combs (as computed via the LLE) should happen simultaneously. We numerically reproduce the near-threshold behavior presented in Fig. 3 of the main text. The result of the combined LLE and input-output theory simulation is presented in Fig. S1a. The modes $\mu = \pm 5$ indeed exit the regime of validity of the input-output formalism (when Q_{eff} has positive real eigenvalues) at the onset of the LLE threshold. Although coherent comb light is present in other modes above threshold, only $\mu = \pm 5$ modes cannot be simulated with the presented linearization approach. A qualitative agreement between simulation and experimentally measured correlations (shown in Fig. 3b of the main text) is seen at the simulated detuning of -9.3 MHz, Fig. S1c.

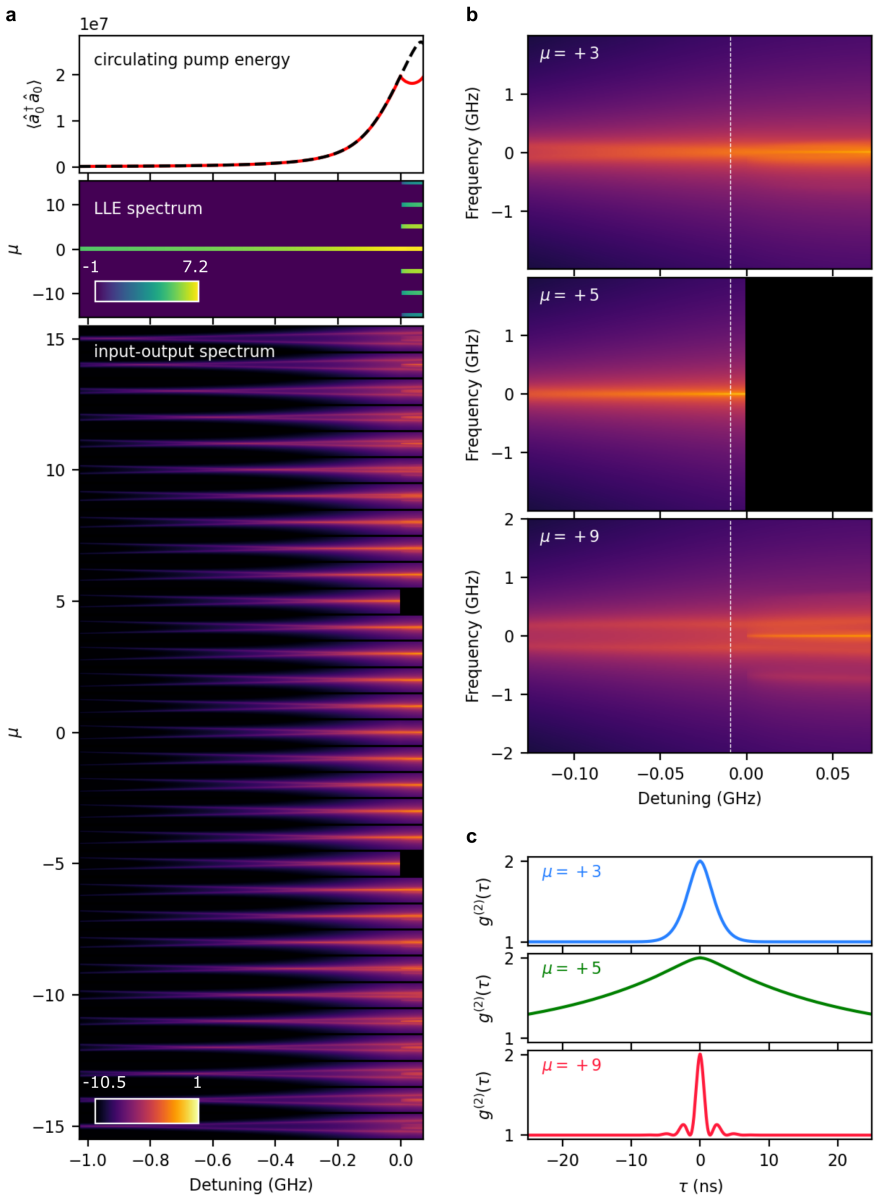

FIG. S1: **Numerical analysis of OPO threshold a** *Top:* Dependence of the pump intensity in the microring (in units of photon number) on laser detuning. Detuning is given relative to the OPO threshold; a higher laser frequency corresponds to a more negative detuning with respect to the OPO condition. The LLE simulation (red) matches the analytic expression for the cavity mode in the presence of the Kerr nonlinear resonance shift (dashed black line) up to the threshold point, where the pump mode becomes depleted. *Middle:* Spectrum of the classical Kerr comb in the ring resonator, computed via the LLE, showing the formation of the 5-FSR primary comb. The scale represents $\log_{10}$(# of photons). *Bottom:* The photon spectrum of the below-threshold modes computed via input-output theory. For each mode, a spectral window of ± 2 GHz is shown. At threshold, modes $\mu = \pm 5$ exit the regime of validity of the linearized model and are excluded from the input-output simulation. The scale represents photon number spectral density, $\log_{10}$(# of photons per Mrad/second). **b** Evolution of the spectrum of three select modes near threshold (same scale as *(b)*). Above threshold, the spectra exhibit additional features generated by the additional parametric processes driven by the primary comb lines. **c** Computed $g^{(2)}_{\text{auto}}(\tau)$ at a detuning of -9.3 MHz (indicated as a dashed line in *(b)*).

E. Second-order photon correlations in merging secondary combs

In this section we describe the modelling of the interference in $g^{(2)}(\tau)$ of stimulated and spontaneous FWM presented in Fig. 4 of the main text. The operator $\hat{b}_{\rm out}(t)$ is:

$$\hat{b}_{\rm out}(t) = \hat{b}_{\rm in}(t) - i\sqrt{\kappa}[\alpha(t) + \hat{a}(t)], \tag{16}$$

or, in the frequency domain,

$$\hat{b}_{\rm out}(\omega) = N(\omega)\hat{b}_{\rm in}(\omega) - i\sqrt{\kappa}\alpha(\omega). \tag{17}$$

Since the coherent field in the mode is bichromatic,

$$\alpha(t) = A_{\rm coh,1}e^{-i\omega_1 t} + A_{\rm coh,2}e^{-i\omega_2 t}. \tag{18}$$

We note that in the presence of a bichromatic coherent state, there is a distinction between $g^{(2)}(\tau)$ and the experimentally-measured correlations. Specifically, the measured correlations are the time-averaged two-photon coincidences $G^{(2)}(\tau) = \left\langle G^{(2)}(t+\tau, t)\right\rangle_t$, normalized to the mean value at $\tau \to \infty$:

$$g^{(2)}_{\rm exp}(\tau) = \frac{\int_{-\infty}^{\infty} G^{(2)}(t+\tau, t)\,{\rm d}t}{\lim_{T\to\infty}\int_T^{\infty}\int_{-\infty}^{\infty} G^{(2)}(t+\tau, t)\,{\rm d}t\,{\rm d}\tau} \tag{19}$$

To model the $g^{(2)}_{\rm exp}(\tau)$ presented in Fig. 4 of the main text, we consider a system of three coherent drives (A_{-8}, A_0, A_{+8}), and four quantum modes ($\hat{a}_{-12}, \hat{a}_{-4}, \hat{a}_4, \hat{a}_{12}$). The effect of other coherent driving modes is assumed negligible, because their amplitude is much smaller. The fit parameters in the model are: 1) two pump amplitudes (A_0, and $A_{+8} = A_{-8}$); 2) two coherent state amplitudes ($A_{\rm coh,1}$ and $A_{\rm coh,2}$); 3) two coherent state frequencies (ω_1 and ω_2); and 4) the pump laser detuning δ_p. The fit is presented in Fig. 4, state 3a of the main text.

F. Characterizing entanglement between cavity modes in soliton crystals

Denoting the modes under consideration by a_μ for $\mu \in \{1, 2 \ldots N\}$ and assuming a quadratic Hamiltonian. In steady state ($t \to \infty$), the density matrix describing any two modes α and β is described by a Gaussian Wigner function:

$$W_{\alpha,\beta}(q_{\alpha,\beta} = [x_\alpha, p_\alpha, x_\beta, p_\beta]^T) = \frac{1}{\pi\sqrt{{\rm Det}[\Sigma_{\alpha,\beta}]}}\exp\left(q^T_{\alpha,\beta}\Sigma_{\alpha,\beta}q_{\alpha,\beta}\right) \tag{20}$$

where $\Sigma_{\alpha,\beta} = \langle q_{\alpha,\beta}q^T_{\alpha,\beta}\rangle_W$ is the 4×4 steady state correlation matrix formed from weyl ordered operators. The entanglement measure between these two modes can be computed as a log-negativity of this matrix, defined by

$$\mathcal{E}_{\alpha,\beta} = \max[0, -\log(\sqrt{2}\eta)] \tag{21}$$

where

$$\eta = \sqrt{\Theta - \sqrt{\Theta^2 - 4{\rm Det}(\Sigma_{\alpha,\beta})}} \tag{22}$$

and

$$\Theta = {\rm Det}(\Sigma_\alpha) + {\rm Det}(\Sigma_\beta) - 2{\rm Det}(C) \tag{23}$$

and $\Sigma_\alpha, \Sigma_\beta$ and C are defined as different blocks of $\Sigma_{\alpha,\beta}$

$$\Sigma_{\alpha,\beta} = \begin{bmatrix}\Sigma_\alpha & C\\ C^T & \Sigma_\beta\end{bmatrix} \tag{24}$$

To compute the correlation matrix $\Sigma_{\alpha,\beta}$ from a quadratic Hamiltonian, it is convenient to express the correlation elements in terms of annihilation operators. We can immediately note that

$$\langle x_\alpha x_\beta \rangle_W = \frac{1}{2}\Big[\langle a_\alpha a_\beta\rangle + \langle a_\alpha^\dagger a_\beta^\dagger\rangle + \langle a_\alpha^\dagger a_\beta\rangle + \langle a_\alpha a_\beta^\dagger\rangle\Big] \tag{25a}$$

$$\langle p_\alpha p_\beta \rangle_W = -\frac{1}{2}\Big[\langle a_\alpha a_\beta\rangle + \langle a_\alpha^\dagger a_\beta^\dagger\rangle - \langle a_\alpha^\dagger a_\beta\rangle - \langle a_\alpha a_\beta^\dagger\rangle\Big] \tag{25b}$$

$$\langle x_\alpha p_\beta \rangle_W = \langle p_\beta x_\alpha \rangle_W = \frac{i}{2}\Big[\delta_{\alpha,\beta} + \langle a_\alpha^\dagger a_\beta^\dagger\rangle - \langle a_\alpha a_\beta\rangle + \langle a_\beta^\dagger a_\alpha\rangle - \langle a_\beta a_\alpha^\dagger\rangle\Big] \tag{25c}$$

The correlators for the annihilation operators required above can be easily calculated from the input-output formalism. Recall that for a quadratic, time-invariant Hamiltonian, the Heisenberg equations read

$$\frac{d}{dt}\begin{bmatrix} a(t) \\ a^\dagger(t)\end{bmatrix} = Q_{\text{eff}}\begin{bmatrix} a(t) \\ a^\dagger(t)\end{bmatrix} + M\begin{bmatrix} b_{in}(t) \\ b_{in}^\dagger(t)\end{bmatrix} \tag{26}$$

Physically, we expect eigenvalues of Q_{eff} to all have negative real part so as to have a well defined steady state. We then obtain by integrating the above equations that as $t \to \infty$

$$\begin{bmatrix} a(t) \\ a^\dagger(t)\end{bmatrix} = \int_0^t e^{Q_{\text{eff}}(t-\tau)} M\begin{bmatrix} b_{in}(\tau) \\ b_{in}^\dagger(\tau)\end{bmatrix} d\tau = \int_0^t X e^{\Lambda(t-\tau)} X^{-1} M\begin{bmatrix} b_{in}(\tau) \\ b_{in}^\dagger(\tau)\end{bmatrix} d\tau \tag{27}$$

where we can define the eigenvalue decomposition $Q_{\text{eff}} = X\Lambda X^{-1}$. It is now straightforward to calculate

$$\lim_{t\to\infty}\langle \begin{bmatrix} a(t) \\ a^\dagger(t)\end{bmatrix}\begin{bmatrix} a^\dagger(t) & a(t)\end{bmatrix}\rangle = \lim_{t\to\infty}\int_0^t X e^{\Lambda(t-\tau)} X^{-1} M M^\dagger X^{-\dagger} e^{\Lambda^*(t-\tau)} X^\dagger d\tau = XNX^\dagger \tag{28}$$

where N is a matrix whose elements are given by

$$N_{i,j} = \frac{[X^{-1}MJM^\dagger X^{-\dagger}]_{i,j}}{\lambda_i + \lambda_j^*} \tag{29}$$

defined in terms of the eigenvalues of Q_{eff}, λ_i, where J is a $2N \times 2N$ matrix:

$$J = \left[\begin{array}{c|c} I(N) & 0 \\ \hline 0 & 0\end{array}\right]$$

II. EXPERIMENTAL SETUP

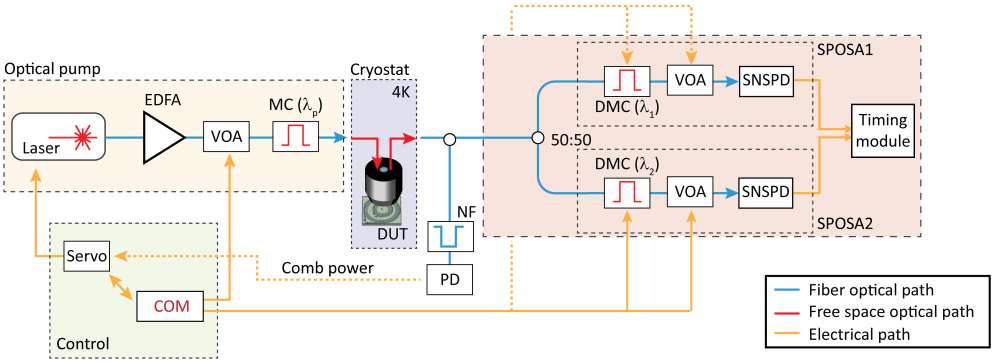

FIG. S2: **Single-photon OSA** Experimental setup. A silicon carbide microring resonator interfaced with inverse-designed vertical couplers[S4] is mounted in a closed-cycle cryostat. Automated locking of a desired microcomb state is performed using active feedback by controlling the laser wavelength and power. A free-space tunable two-pass monochromator (MC) and double monochromator (DMC) serve as narrow band-pass filters with rejection of >130 dB and >180 dB, respectively. The dynamic range of the superconducting nanowire single photon detectors (SNSPDs) is extended from 60 dB to 180 dB via variable optical attenuators (VOA). A single SPOSA is used for spectroscopy and two SPOSAs are used for photon correlation measurements. Photon detection events are recorded with a timing module TimeTagger Ultra from Swabian Instruments.

III. SILICON CARBIDE SOLITON MICROCOMB

In this section, we describe the first demonstration of a soliton microcomb in a 4H-silicon carbide (SiC) microresonator. The CMOS-compatible fabrication process is described in[S4,S5]. SiC possesses a high linear and nonlinear refractive indices[S4] ($n = 2.6$ and $n_2 = 6.9 \cdot 10^{-15}$ cm^2/W at 1550 nm), which makes it suitable for highly efficient, compact nonlinear photonic devices. However, the tight confinement and high material index of integrated waveguides make them susceptible to scattering losses caused by surface roughness. We demonstrate the fabrication of SiC microresonators with smooth sidewalls and strong confinement with record-high quality (Q) factors. The fabricated microring resonators have a radius of 100 µm, height of 500-600 nm, and width of 1850 nm.

A. Sub-mW parametric oscillation threshold

The efficiency of the Kerr nonlinear interaction improves with higher quality factors of the optical resonator. For example, the threshold relation for optical parametric oscillation in a microresonator can be expressed in the following form:

$$P_{th} = \frac{\pi n \omega_0 A_{\text{eff}}}{4\eta\, n_2} \frac{1}{D_1 Q^2} \tag{30}$$

where Q denotes the total Q factor (intrinsic loss and loading included) with pump mode frequency ω_0, A_{eff} is the effective mode area, η is the cavity-waveguide coupling strength, and D_1 is the free-spectral range (FSR) in units of rad/s. Zero detuning of the laser frequency with respect to the pump mode frequency is assumed. The parametric oscillation threshold is inversely proportional to the square of the Q factor. Fig. S3 shows a sub-milliwatt (approximately 510 µW) parametric oscillation threshold of a SiC optical resonator featuring an intrinsic Q factor of 5.6 million with a 350 GHz FSR.

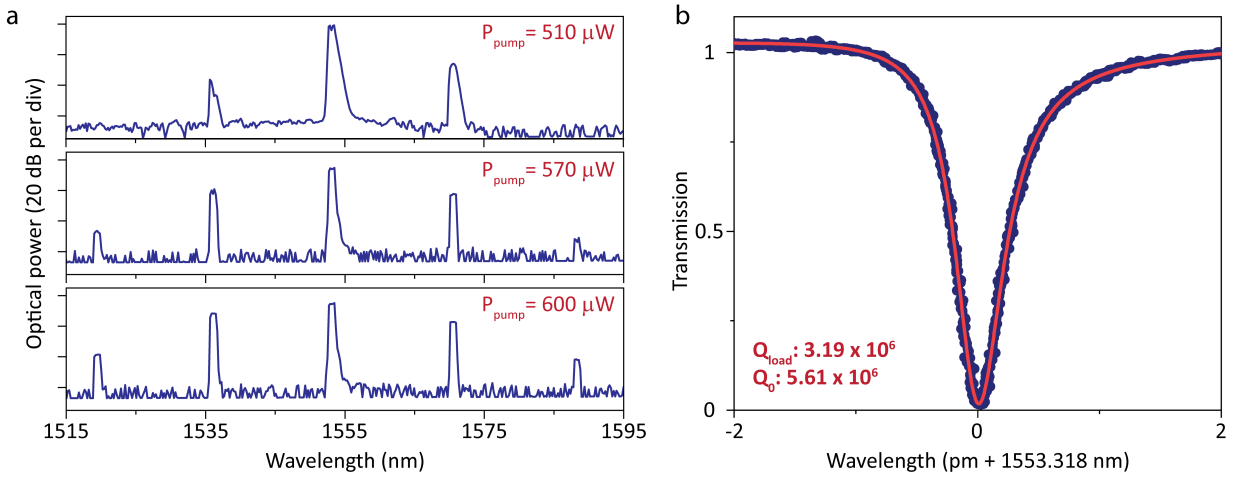

FIG. S3: **Sub-mW parametric oscillation threshold power** (**a**) SiC parametric oscillation induced by pumping at the wavelength of 1553.3 nm. Top panel shows OPO just above the threshold power (510 µW total power in the waveguide). Middle and lower panels show measured optical spectra with loaded pump power of approximately 570 and 600 µW, respectively. (**b**) High-resolution scan of the fundamental TE mode with a loaded (intrinsic) quality factor of 3.19 (5.61) million. The mode is seen to be nearly critically-coupled to the waveguide. The scan laser wavelength is calibrated using a wavemeter, and the red curve is a fit to a Fano lineshape. The asymmetry of the resonance shape is attributed to interference with back-reflection of the vertical couplers.

B. Demonstration of a Silicon Carbide soliton microcomb

Coherently pumped solitons in optical microresonators form as a result of the balance of the Kerr nonlinear shift and the cavity dispersion, as well as the parametric gain and the cavity loss. The soliton-forming mode family (in particular for bright solitons) in a microresonator must feature anomalous dispersion and minimal distortion of the dispersion

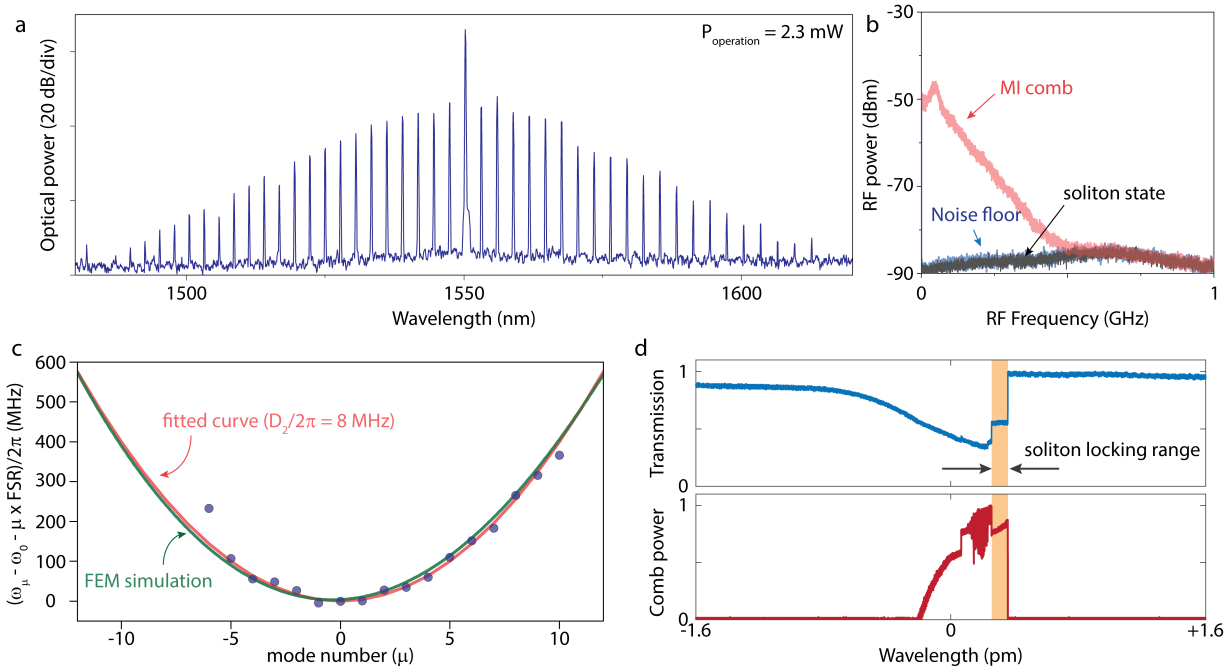

FIG. S4: **SiC soliton microcomb** (**a**) The optical spectrum of a single soliton state with 2.3 milliwatts operation power. (**b**) RF spectrum (resolution bandwidth = 100 kHz) of the entire soliton comb confirms a low-noise state. (**c**) Measured frequency dispersion belonging to the soliton forming mode family (TE_{00}) is plotted versus the relative mode number. The red curve is a fit using $D_1/2\pi = 358.663$ GHz and $D_2/2\pi = 8$ MHz. Simulation of the soliton mode families is plotted (green curve), and the simulation fairly agrees with the measurement results. (**d**) Upper panel presents pump power transmission versus tuning across a resonance used for the soliton formation. Lower panel shows comb power trace in which the pump laser scans over the resonance from the short wavelength (blue detuned) to the long wavelength (red detuned). The shaded region (orange) depicts the spectral region where the single soliton exists.

(*e.g.*, minimal avoided-mode-crossings). The power requirement for soliton operation is inversely proportional to the total Q factor of the mode family[S6].

We demonstrate the generation of a dissipative soliton microcomb in a SiC microresonator. Figure S4a shows the spectrum measured for a single-soliton state, and the soliton spectral shape follows the square of a hyperbolic secant function. Small spurs in the spectrum correlate with the avoided-mode-crossings in the mode dispersion spectrum (Fig. S4c), and the RF spectrum of the single-soliton state confirms that it is a low-noise state (Fig. S4b). While tuning the laser through the resonance mode, the pump power transmission as well as the comb power (Fig. S4d) show a step transition from modulation instability (MI) and a chaotic comb state to a stable soliton comb state. The high Q SiC resonator enables a low operation power of the soliton microcomb of 2.3 mW: Table I compares operation powers of various chip-scale soliton devices.

Material	**Q_0 (M)**	**FSR (GHz)**	**Soliton operation power (OPO threshold) (mW)**	**Reference**
Si_3N_4	260	5	$\sim$ 20	Ref [S7]
Si_3N_4	8	194	1.3 (1.1)	Ref [S8]
Si_3N_4	15	99	6.2 (1.7)	Ref [S9]
SiO_2/Si_3N_4	120	15	28 (5)	Ref [S10]
$LiNbO_3$	2.4	199.7	5.2	Ref [S11]
AlGaAs	1.5	450	1.77 (0.07)	Ref [S12]
SiC	5.6	350	2.3 (0.51)	This work

TABLE I: **Comparison of integrated soliton device performance**

IV. SOLITON CRYSTALS

Soliton crystals, temporally-ordered ensembles of soliton pulses, have been observed in various optical resonator platforms, and their dynamics as well as defect-free generation have been actively explored. We demonstrate soliton crystal states with 2- and 7-FSR comb spacing, corresponding to phase-locked lattice of 2 and 7 identical solitons, respectively. We characterize the soliton crystals through the analysis of their optical spectra, RF beatnote, and second-order photon correlations.

A. 2-FSR soliton crystal

Figure S5 shows the OSA spectrum and RF beatnote noise of the soliton crystal state that is studied in Fig. 5 of the main text. In the main text, the RF beatnote of a single resonator mode is shown; In Fig. S5, we show the RF spectrum of the whole comb. Sweeping the laser from blue- to red-detuned, we observed a transition from a broad and noisy RF signal corresponding to the modulation instability (MI) state, to a low-noise state, coinciding with the beginning of a discrete step in the transmission trace across the cavity resonance.

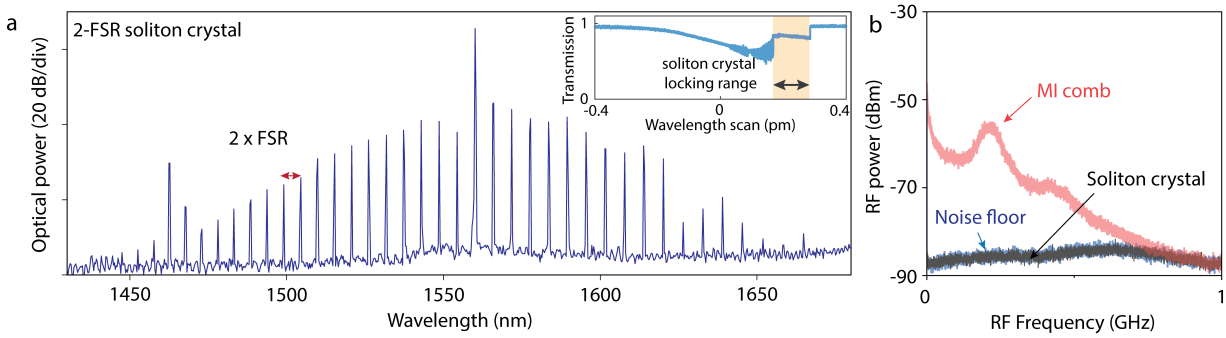

FIG. S5: **2-FSR soliton crystal state** (**a**) OSA spectrum of the soliton crystal state. Inset: pump power transmission versus laser tuning when the pump laser wavelength is scanned from blue- to red-detuned across the pump resonance. (**b**) RF spectra (resolution bandwidth = 100 kHz) of the soliton comb (black) and MI comb (red).

B. Photonic molecule analysis

The second-order correlation matrix for the 2-FSR soliton crystal state (presented in Fig. 5c of the main text) was computed via LLE simulation and input-output theory using the following parameters:

- $D_2/2\pi$ = 3.65 MHz, obtained from FEM simulation, neglecting higher-order terms. A single perturbation of −30 MHz was introduced at mode $\mu = -2$ to induce the formation of the soliton crystal state[S13].
- For the pump mode ($\mu = 0$), the intrinsic and coupling Q factors of 2.37 and 6.55 million, respectively, were used, extracted from the measured cold-cavity transmission spectrum.
- For the other modes, intrinsic and coupling Q of 2.77 and 7.47 million, respectively, were used, corresponding to the mean of the measured Q factors for the modes within the laser scanning range ($\mu = -3$ to $+14$).
- Pump power of 6.6 mW in the waveguide, corresponding to the experimentally-measured value.

The result of the LLE simulation is shown in Fig. S6b. The simulated soliton crystal spectrum for the detuning of 330 MHz is shown in Fig. S6c. In the input-ouput theory model, the laser detuning (within the range of existence of the soliton state in the LLE simulation) is the only free parameter. The corresponding second-order photon correlations and E_N matrices are shown in Fig. S6d. Negligible entanglement is thus predicted in the resonator mode basis for this soliton crystal state. However, entanglement can be recovered by selectively over-coupling the below-threshold modes via a photonic molecule configuration, shown in Fig. S6e. This configuration is as follows: The auxillary resonator has a FSR that is 2 times larger than the FSR of the primary microring. The coupling strength of the two ring resonators exceeds the total losses (scattering and waveguide coupling) of the primary resonator. The auxillary ring is further over-coupled to its output waveguide, so that rather than be strongly-coupled to the primary resonator, the auxillary

resonator acts as a selective out-coupling channel for the odd-numbered modes of the primary resonator. We note that the finesse of the experimentally demonstrated resonators (approximately 3500) is sufficient for this architecture. To model this system, we perform the LLE simulation with the same device parameters as for the experimentally demonstrated device, but with the out-coupling rates of the odd modes increased by 10 times. We numerically confirm that the same 2-FSR soliton state can be prepared for this device (Fig. S6f). The computed second-order correlation and E_N matrices for the the quantum state of this device are shown in Fig. S6h.

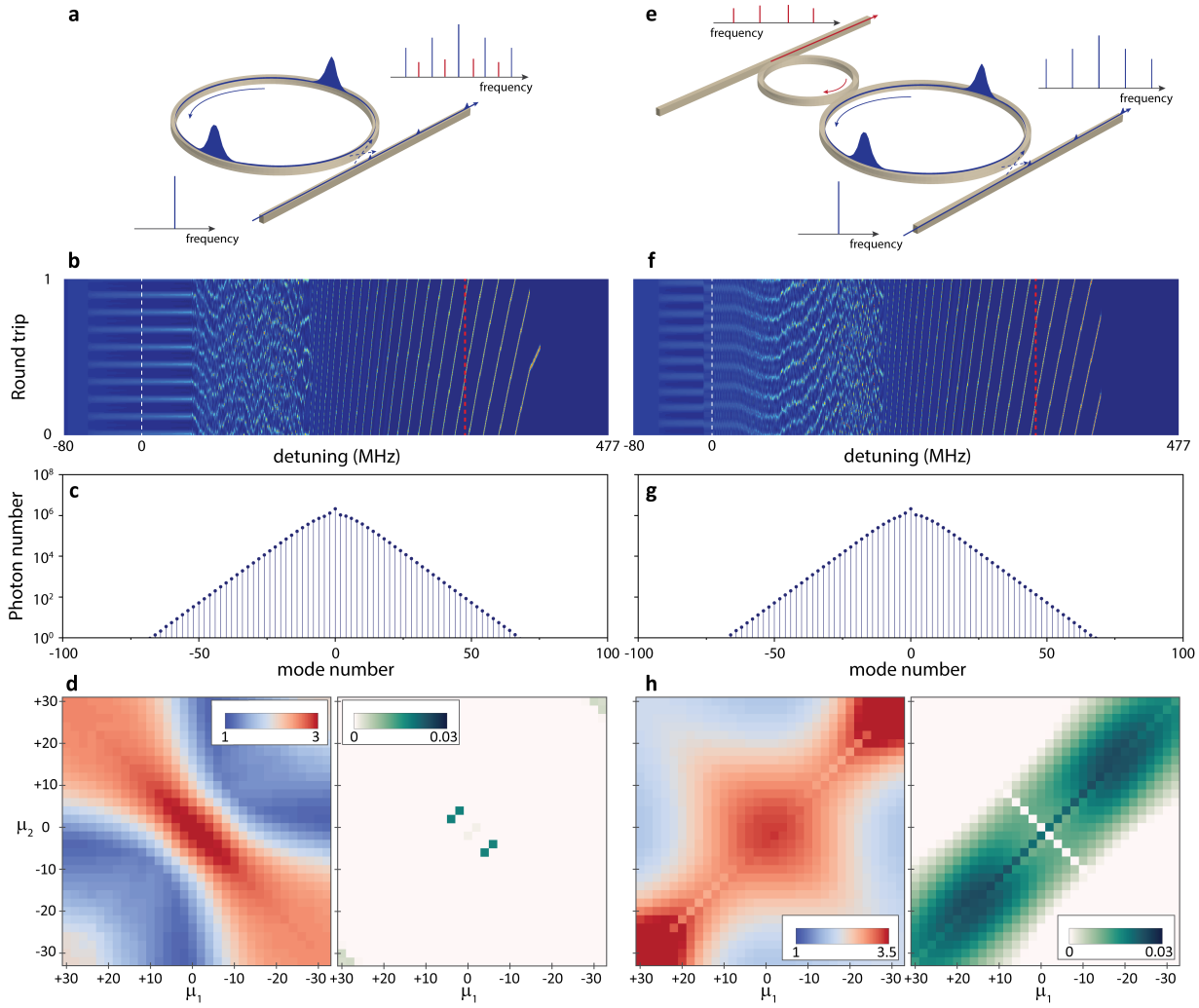

FIG. S6: **Photonic molecule architecture for all-to-all entanglement generation (a)** Schematic of the experimentally-demonstrated device. **(b)** LLE simulation of the device for pump power of 6.6 mW in the waveguide. The desired 2-FSR soliton crystal state exists for detuning in the range 175–395 MHz. This simulated soliton step width of 220 MHz is somewhat larger than the experimentally-observed step width of 150 MHz. **(c)** The simulated spectrum taken at detuning of 330 MHz. **(d)** Left: The two-photon correlation matrix computed for the state in (c). The scale bar indicates $\max\{g^{(2)}(\tau)\}$. Right: The corresponding entanglement negativity, E_N, matrix. (e-h) correspond to (a-d) but for the photonic molecule configuration, where the out-coupling of the odd resonator modes is increased by 10 times via the auxilliary resonator **(e)** Schematic of the photonic molecule configuration. **(f)** It is confirmed via LLE that the same 2-FSR soliton crystal state can be captured in simulation. **(g)** The spectrum of the comb at the same detuning of 330 MHz is identical to the comb spectrum in the unmodified device, since only the below-threshold modes are affected by the addition of the auxiliary ring. **(h)** The corresponding correlation and entanglement matrices for the photonic molecule device.

C. 7-FSR soliton crystal

Figure S7 presents the generation of a 7-FSR soliton crystal state in a different device. The optical spectrum (Fig. S7a) as well as the transmission and comb power traces across the pump resonance identify the existence of the soliton state. The SPOSA spectrum (Fig. S7c) reveals quantum frequency comb lines which were obscured by the noise floor of the OSA spectrum, and their correlation matrix is presented with the prediction from the LLE-driven linearized model (Fig. S7d).

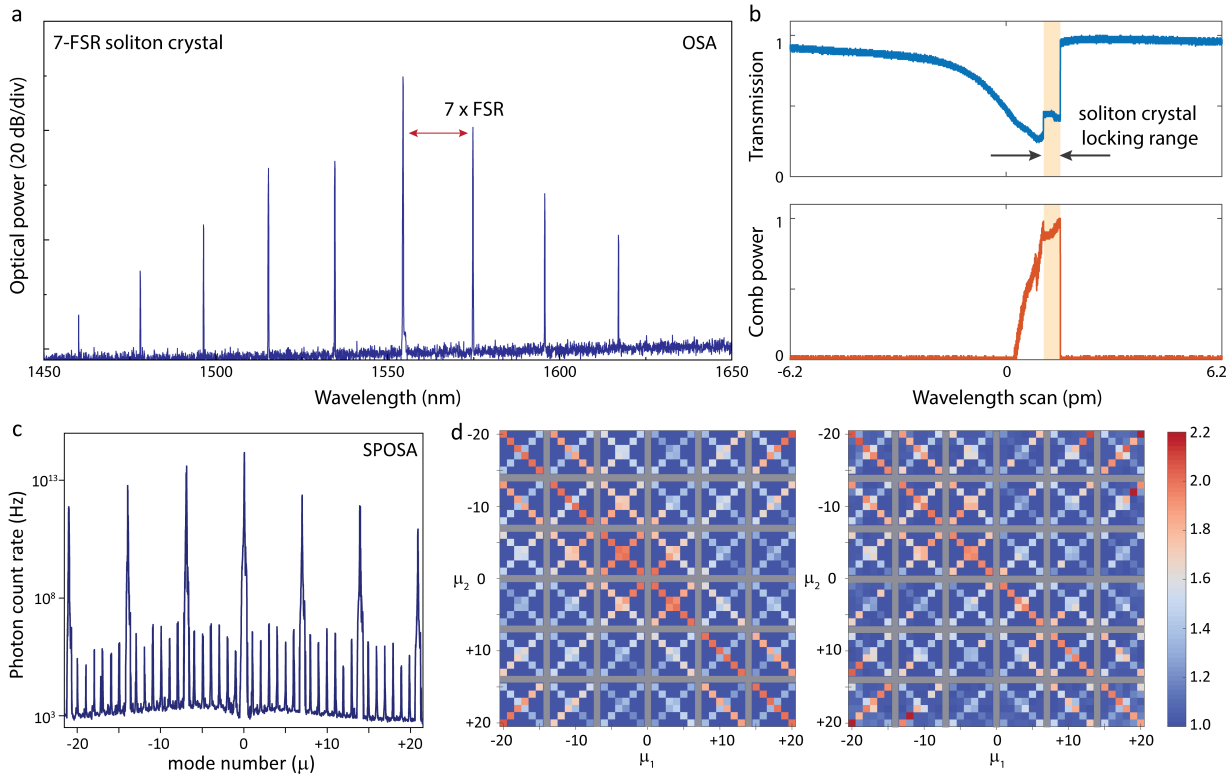

FIG. S7: **7-FSR soliton crystal state** (**a**) OSA spectrum of the soliton crystal state. (**b**) Pump power transmission (upper panel) and comb power (lower panel) versus wavelength tuning when the pump laser is scanned from blue to red across the pump resonance. (**c**) Optical spectrum of the soliton state measured using the SPOSA. (**d**) The max$[g^{(2)}(\tau)]$ correlation matrix for the below threshold modes in the 7-FSR soliton state (Left: theoretical model, Right: experimental data).

[S1] Chembo, Y. K. & Menyuk, C. R. Spatiotemporal lugiato-lefever formalism for kerr-comb generation in whispering-gallery-mode resonators. *Physical Review A* **87**, 053852 (2013).

[S2] Chembo, Y. K. Quantum dynamics of kerr optical frequency combs below and above threshold: Spontaneous four-wave mixing, entanglement, and squeezed states of light. *Physical Review A* **93**, 033820 (2016).

[S3] Ou, Z. & Lu, Y. Cavity enhanced spontaneous parametric down-conversion for the prolongation of correlation time between conjugate photons. *Physical Review Letters* **83**, 2556 (1999).

[S4] Guidry, M. A. *et al.* Optical parametric oscillation in silicon carbide nanophotonics. *Optica* **7**, 1139–1142 (2020).

[S5] Lukin, D. M. *et al.* 4H-silicon-carbide-on-insulator for integrated quantum and nonlinear photonics. *Nature Photonics* **14**, 330–334 (2020).

[S6] Yi, X., Yang, Q.-F., Yang, K. Y., Suh, M.-G. & Vahala, K. Soliton frequency comb at microwave rates in a high-q silica microresonator. *Optica* **2**, 1078–1085 (2015).

[S7] Jin, W. *et al.* Hertz-linewidth semiconductor lasers using cmos-ready ultra-high-q microresonators. *Nature Photonics* 1–8 (2021).

[S8] Stern, B., Ji, X., Okawachi, Y., Gaeta, A. L. & Lipson, M. Battery-operated integrated frequency comb generator. *Nature* **562**, 401–405 (2018).

[S9] Liu, J. *et al.* Ultralow-power chip-based soliton microcombs for photonic integration. *Optica* **5**, 1347–1353 (2018).
[S10] Yang, K. Y. *et al.* Bridging ultrahigh-q devices and photonic circuits. *Nature Photonics* **12**, 297–302 (2018).
[S11] He, Y., Ling, J., Li, M. & Lin, Q. Perfect soliton crystals on demand. *Laser & Photonics Reviews* **14**, 1900339 (2020).
[S12] Chang, L. *et al.* Ultra-efficient frequency comb generation in algaas-on-insulator microresonators. *Nature communications* **11**, 1–8 (2020).
[S13] Karpov, M. *et al.* Dynamics of soliton crystals in optical microresonators. *Nature Physics* **15**, 1071–1077 (2019).